Supplementary Information

Activating *sp* Hybridization of Zinc Iodide via $\pi_{sp\text{-}p}$ Bonding Donation Enables Ah-Level Seawater-based Wearable Zinc-Iodine Pouch Cells

Weina Guo,†[a] Cheng Gu,†[a] Jun Li,†[b] Liufeng Chen,[a] Zhijie Li,[a] Wuxuan Liu,[a] Shuo Wang,[c] Gengzhi Sun,[a] Lin Wang,*[a] Linghai Zhang,*[a] Chenyang Zha,*[ade] and Kwun Nam Hui[e]

[a] Key Laboratory of Flexible Electronics (KLOFE), School of Flexible Electronics (Future Technologies), Institute of Advanced Materials (IAM), Nanjing Tech University, Nanjing, 211816 China

E-mail: iamlwang@njtech.edu.cn (L. Wang); iam.lzhang@njtech.edu.cn (L. Zhang); iamcyzha@njtech.edu.cn (C. Zha)

[b] School of Chemistry and Chemical Engineering, North University of China, Taiyuan, 030051 China

[c] Division of Energy Storage, Dalian Institute of Chemical Physics, Chinese Academy of Sciences, Dalian 116023, China

[d] Guangdong-Hong Kong Joint Laboratory for Carbon Neutrality, Jiangmen Laboratory of Carbon Science and Technology, Hong Kong University of Science and Technology (Guangzhou), Guangzhou, 511453 China

[e] Institute of Applied Physics and Materials Engineering (IAPME), University of Macau, Taipa 999078, Macao SAR, China

E-mail: chenyangzha@um.edu.mo

† These authors contributed equally to this work.

Experimental Section

Electrolyte preparation:

The baseline seawater electrolyte was prepared as an artificial seawater solution containing 0.5 M Li_2SO_4, 0.42 M NaCl, 0.0547 M $MgCl_2 \cdot 6H_2O$, 0.0288 M Na_2SO_4, 2.0 M $ZnSO_4$, 0.0025 M $CaCl_2$, 0.00093 M KCl, 0.00239 M $NaHCO_3$, 0.00085 M KBr, 0.000437 M H_3BO_3, 0.000158 M $SrCl_2 \cdot 6H_2O$, and 0.0000714 M NaF. All components were dissolved through magnetic stirring until a clear, homogeneous solution was obtained. For the modified electrolytes, 1,3-dioxane (1,3-DX) was introduced into the seawater electrolyte at 2, 4, 6, 8, and 10 vol% (corresponding to 0.2346, 0.4693, 0.7039, 0.9386, and 1.1733 M, respectively). Both the 1,3-DX-free seawater electrolyte and the optimized 6 vol% 1,3-DX-modified electrolyte were formulated for comparative evaluation.

Cathode preparation:

The iodine-containing catholyte (1.2 M) was prepared by dissolving 1 M LiI and 0.1 M I_2 in ethanol, followed by magnetic stirring at 25 ^oC for 2 h to obtain a homogeneous solution. The use of ethanol ensures good solubility and molecular-level mixing of LiI and I_2, forming a stable iodide redox medium. This homogeneous precursor solution is essential for achieving uniform iodine distribution during subsequent loading. For electrode fabrication, the catholyte was introduced into the carbon host using a micropipette in a controlled, stepwise manner. Specifically, a small and fixed volume of catholyte was dispensed onto the electrode surface in each cycle, allowing sufficient time for capillary-driven infiltration into the pore network before

drying. After each addition, the electrode was dried under ambient conditions to ensure complete evaporation of ethanol. The mass of the electrode was carefully measured after each drying step, and the impregnation-drying cycle was repeated until the desired iodine loading was reached. This gradual loading strategy avoids oversaturation of the surface and promotes uniform penetration of iodine species throughout the internal structure rather than accumulation on the surface. As a result, iodine is evenly distributed within the carbon matrix, which was also confirmed by the good reproducibility of electrode mass gain and electrochemical performance. Regarding solvent evaporation and iodine stability, ethanol was selected due to its moderate volatility, which enables relatively slow and controlled evaporation. This prevents rapid supersaturation and local precipitation of iodine that could otherwise lead to inhomogeneous distribution. Importantly, drying was performed at room temperature without additional heating, thereby minimizing the risk of iodine sublimation. Furthermore, the presence of excess iodide ions promotes the formation of nano-scale iodine materials, which have significantly higher electrochemical activity compared to bulk iodine. Overall, the combination of a homogeneous catholyte, stepwise impregnation with precise mass control, controlled solvent evaporation, and chemical stabilization of iodine ensures uniform and reproducible iodine distribution while minimizing iodine loss. The cathode of Zn-MnO_2 cell is assembled by mixing 70 wt% commercial MnO_2, 20wt% Super P and 10 wt% polyvinylidene fluoride (PVDF) which are dispersed in 1 mLN-Methyl pyrrolidone (NMP). The slurry is stirred by magnetic force for 24 h andvacuum drying at 70 °C for 6 h after covering on the Ti foil. The active material loading is around 0.3-2 mg/cm^2.

Anode preparation:

The Zn foils (99 %, 100 μm thick) were mechanically polished with sandpaper and subsequently cleaned by ultrasonic treatment in ethanol to remove surface oxides and residual contaminants. The cleaned foils were then cut into sheet-like electrodes of the required dimensions for use as Zn anodes.

Pouch cell assembly:

All pouch-cell assembly and disassembly procedures were performed under ambient atmospheric conditions. Glass fiber paper (Whatman GF/A) was used as the separator. The assembled Zn-I_2 pouch cells were subsequently subjected to electrochemical characterization. A pre-formed aluminum-laminate pouch was first cleaned with ethanol and thoroughly dried. The cathode, separator, and Zn anode were stacked into a sandwich-type configuration and then placed into the pouch, ensuring that all current-collecting tabs were aligned and extended smoothly from the sealing edges. The pouch was then partially sealed on three sides, leaving one designated electrolyte-filling port unsealed. The electrolyte was injected into the pouch cell through the filling port using a low vacuum-sealing system. After injection, the cell was maintained under vacuum for an additional 5-10 min to ensure full infiltration of the electrolyte and complete wetting of the electrodes and separator. Finally, the filling port was heat-sealed to obtain a fully enclosed pouch cell. In the folding test, graphene oxide (0.4 mg/mL) is incorporated into the seawater electrolyte to enhance the mechanical integrity of the zinc electrode, ensuring structural stability during repeated bending and deformation.

Material characterization:

X-ray diffraction (XRD) patterns were recorded using a SmartLab Rigaku diffractometer to determine the crystalline structure of the materials. Morphological analysis at the micrometer scale was conducted using a JSM-7610F Plus scanning electron microscope (SEM). Raman spectra were collected using a Zolix Finder Smart FST2-MPL501-405C1 micro-Raman spectroscopy system to probe molecular interactions and structural features. The X-ray photoelectron spectroscopy (XPS) measurements were carried out on a Thermo Scientific Nexsa XPS system with a monochromatic Al Kα radiation ($h\nu$ = 1486.7 eV) and a concentric hemispherical analyzer. Core peaks were analyzed using a nonlinear Shirley-type background, and peak positions and areas were obtained by a weighted least-squares fitting of model curves. All XPS data analysis were carried out using Avantage software.

Electrochemical measurements:

Cyclic voltammetry (CV) measurements were performed on a CHI600e electrochemical workstation. Long-term cycling performance was assessed using a NEWARE battery testing system, and 1 C corresponds to 200 mA/g. Electrochemical impedance spectroscopy (EIS) was carried out on a Gamry potentiostat with a 10 mV AC perturbation over the frequency range of 100 kHz to 10 mHz. Electrochemical stability was assessed using Zn//Zn symmetric cells at room temperature. Coulombic efficiency (CE) was measured using Zn//Cu asymmetric cells with a cutoff voltage of 0.6 V. For the Zn//Zn symmetric cells, Zn foil with a thickness of 50 μm and a diameter of 12 mm was used as the anode. In Zn//Cu asymmetric cells, the Zn foil anode also had a diameter of 12 mm, while the Cu foil cathodes had a diameter of 16 mm.

Relative texture coefficients characterization:

The microstructure of the electroplated films before and after self-annealing was characterized. The grain orientation of the films was characterized by XRD. Based on the XRD results, the relative texture coefficients (RTC) were calculated as follows:

$$\text{RTC}\ (hi\ ki\ li) = \frac{I\ (hi\ hi\ hi)}{I_0\ (hi\ hi\ hi)} \frac{1}{N} \sum_{i=1}^{N} \left(\frac{I\ (hi\ hi\ hi}{I_0(hi\ hi\ hi)}\right)_{-1}$$

where I (*hi hi hi*) is the intensity of the (*hi hi hi*) diffraction peak of the samples under investigation, I_0 (*hi hi hi*) is the intensity of the (*hi hi hi*) plane of the standard sample taken from the powder diffraction file card, and N is the number of diffractions in the analysis.

Calculation methods:

First-principles calculations were performed using the Vienna *Ab*-initio Simulation Package (VASP).[S1-S4] The exchange-correlation interactions were treated within the Generalized Gradient Approximation (GGA) using the Perdew-Burke-Ernzerhof (PBE) functional.[S1-S4] A plane-wave basis set with a cutoff energy of 450 eV was employed to expand the electronic wave functions. The Brillouin zone was sampled using a 3 x 1 x 1 Monkhorst-Pack k-point mesh within the Γ-centered scheme.[S1-S4] The ionic cores were treated using the projector augmented wave (PAW) method with an energy cutoff of 400 eV.[S1-S4] The Zn (002), (100), and (101) surfaces were modeled by cleaving the bulk Zn structure, with a vacuum layer of approximately 16 Å along the c-axis to avoid interactions between periodic images. Adsorption energies were

calculated as E_{ads} = E(adsorbate/surface) – E(adsorbate) – E(surface), where E(surface), E(adsorbate), E(adsorbate/surface) are the total energies of the clean Zn surface, the isolated adsorbate (1,3-DX, H_2O), and the adsorbate on the surface, respectively. To account for van der Waals interactions, Grimme's DFT-D2 correction was applied. [S1-S4] To provide an intuitive picture of interfacial charge transfer, we calculated the charge density difference using the following expression: $\Delta\rho = \rho$(adsorbate/surface) − ρ (surface) – ρ(adsorbate), where ρ(surface), ρ(adsorbate), and ρ(adsorbate/surface) represent the charge densities of clean Zn surface, the isolated adsorbate, and the adsorbate on the surface.[S1-S4] The $ZnSO_4$-dioxane-water electrolyte systems were constructed using molecular dynamics (MD) simulations.[S5-S6] Mixed electrolytes were generated with the Disordered System Builder, where the numbers of $ZnSO_4$, 1,3-DX, and water molecules were determined by the target molarities, simulation volume, and the standard molarity of water, ensuring accurate solution stoichiometry. The OPLS-AA force field was applied to all components, with TIP3P used for water. Zn^{2+} ions were assigned non-coordinating parameters to allow their hydration and sulfate interactions to evolve freely during the simulation. Long-range electrostatics were computed using the Particle Mesh Ewald method, and the van der Waals cutoff distance was set to 9.0 Å. Before production runs, each system underwent energy minimization followed by a multistage equilibration protocol. This included an initial NVT step to remove high-energy local configurations, an NPT density relaxation at 300 K and 1 atm until the total energy and density stabilized, and a gradual release of positional restraints to reach an unconstrained dynamical state. A 50-ns NPT production simulation was then performed with a 2-fs timestep. Temperature and pressure were controlled using the Nosé-Hoover thermostat and Martyna-Tobias-Klein barostat. Prior to analysis, trajectories were unwrapped and centered to eliminate periodic artifacts. Radial

distribution functions and coordination numbers were evaluated to characterize the local solvation structure of Zn^{2+} with respect to the oxygen atoms of water, sulfate, and dioxane. Coordination numbers were obtained by integrating to the first local minimum of each radial distribution function, corresponding to the boundary of the primary solvation shell. [S7-S9] Reduced density gradient (RGD), Frontier molecular orbital, the distribution of electrons and holes in the electron excitation process, and interfragmentary charge transfer were calculated with Multiwfn 3.8 (dev). Molecular dynamics simulation, conducted using CP2K software.[S9-S10]

References:

[S1] G. Kresse, J. Furthmüller, Efficient iterative schemes for ab initio total-energy calculations using a plane-wave basis set, Phys. Rev. B 54 (16) (1996) 1116911186.

[S2] J.P. Perdew, K. Burke, M. Ernzerhof, Generalized Gradient Approximation Made Simple, Phys. Rev. Lett. 77 (18) (1996) 3865-3868.

[S3] P.E. Blöchl, Projector augmented-wave method, Phys. Rev. B: Condens. Matter Mater. Phys. 50 (24) (1994) 17953-17979. S. Grimme, Semiempirical GGA-type density functional constructed with a long-range dispersion correction, J. Comput. Chem. 27 (15) (2006) 1787-1799.

[S4] G. Henkelman, H. Jónsson, Improved tangent estimate in the nudged elastic band method for finding minimum energy paths and saddle points, J. Chem. Phy. 113 (22) (2000) 9978-9985.

[S5] M. J. Abraham, T. Murtola, R. Schulz, S. Páll, J. C. Smith, B. Hess, E. Lindahl, GROMACS: High performance molecular simulations through multi-level parallelism from laptops to supercomputers. SoftwareX 1-2 (2015) 19-25.

[S6] H. J. C. Berendsen, J. R. Grigera, T. P. Straatsma, The missing term in effective pair potentials. J. Phys. Chem. 91 (1987) 6269-6271.

[S7] W. L. Jorgensen, D. S. Maxwell, J. Tirado-Rives, Development and Testing of the OPLS All-Atom Force Field on Conformational Energetics and Properties of Organic Liquids. J. Am. Chem. Soc. 118 (1996) 11225-11236.

[S8] W. Humphrey, A. Dalke, K. Schulten, VMD: Visual molecular dynamics. J. Mol. Graph. 14 (1996) 33-38.

[S9] Lefebvre, C.*, et al.* Accurately extracting the signature of intermolecular interactions present in the NCI plot of the reduced density gradient versus electrondensity. *Physical Chemistry Chemical Physics* **19**, (2017) 17928-17936.

[S10] Lu, T. & Chen, F. Multiwfn: A multifunctional wavefunction analyzer. *Journal of Computational Chemistry* **33**, (2012) 580-592.

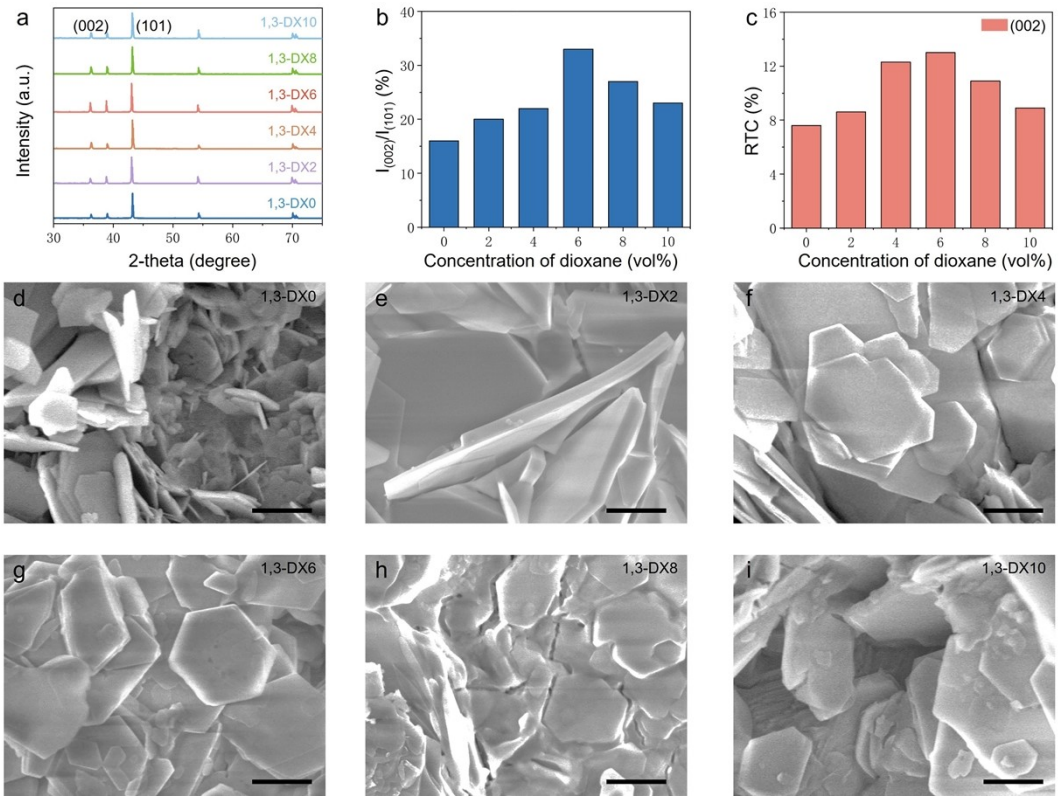

Fig. S1. Structural characterization of seawater electrolytes with varying concentrations of 1,3-DX. XRD pattern (a) of the cycled Zn//Zn cells with the corresponding peak intensity of (002)/(101) facets (b), and RTC of (002) facets (c). The corresponding SEM images (d-i), and bar scale is 1 μm.

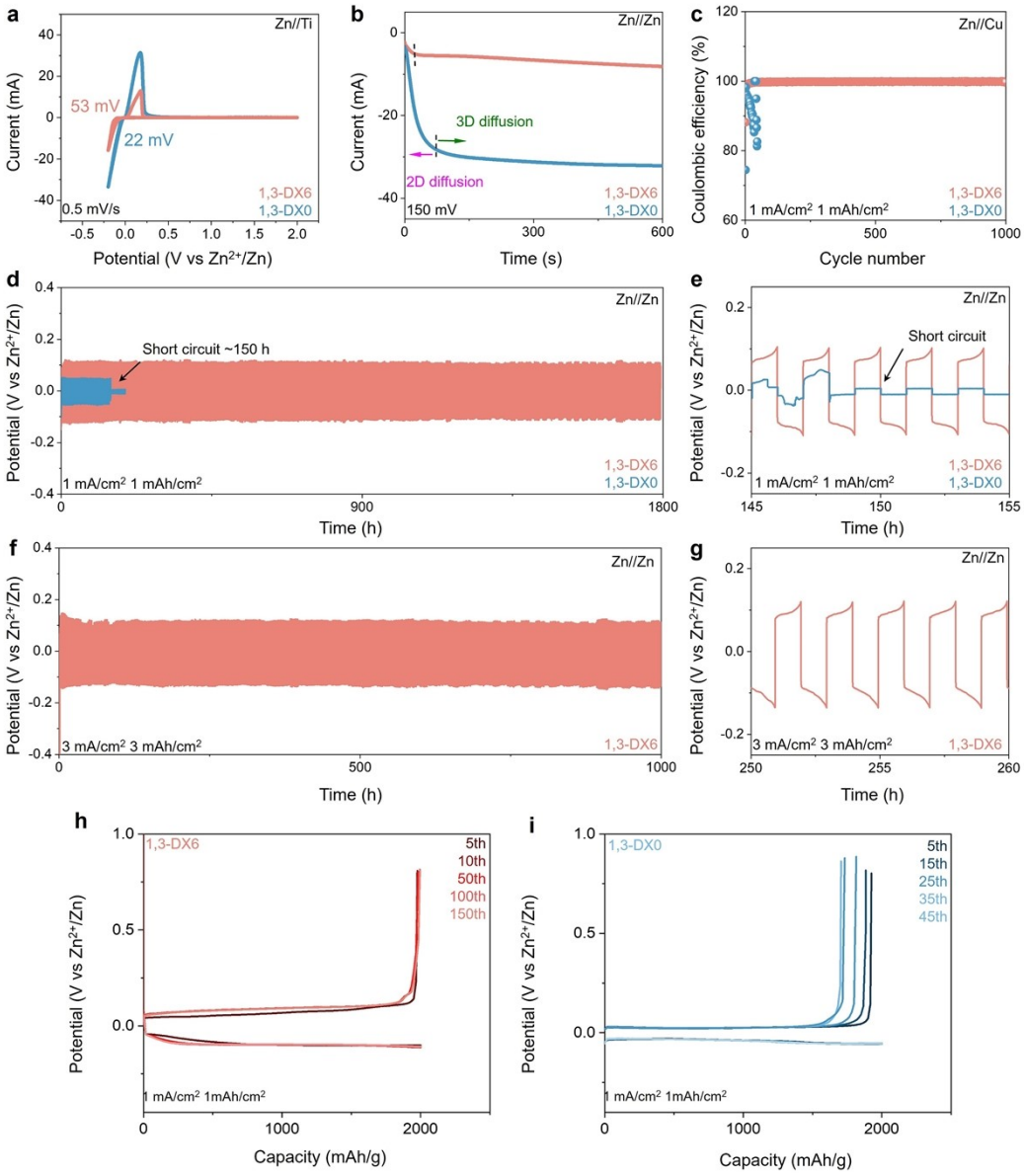

Fig. S2. Electrochemical performance of seawater electrolytes with varying concentrations of 1,3-DX. The CV curves of Zn//Ti cells (a), CA curves of Zn//Zn cells (b), and Coulombic efficiency of Zn//Cu cells (c). The Zn//Zn symmetric cells of voltage profiles at 1 mA/cm^2 under 1 mAh/cm^2 (d-e), and 3 mA/cm^2 under 3 mAh/cm^2 (f-g). The corresponding voltage profiles of Zn//Cu cells with 1,3-DX6 and 1,3-DX0 at different cycling (h-i), respectively.

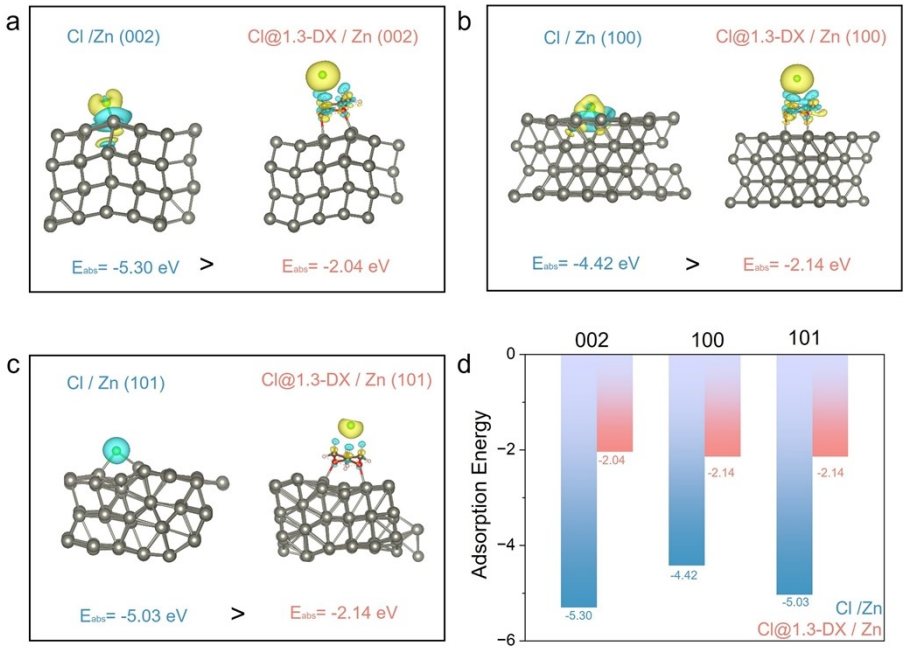

Fig. S3. Theoretical investigation of 1,3-DX as an electrolyte catalyst for regulating Zn anode mechanisms. Binding energy (a-c) of Cl^- or Cl^--1,3-DX on the Zn (002), (100), and (101) facets, and the corresponding summary (d).

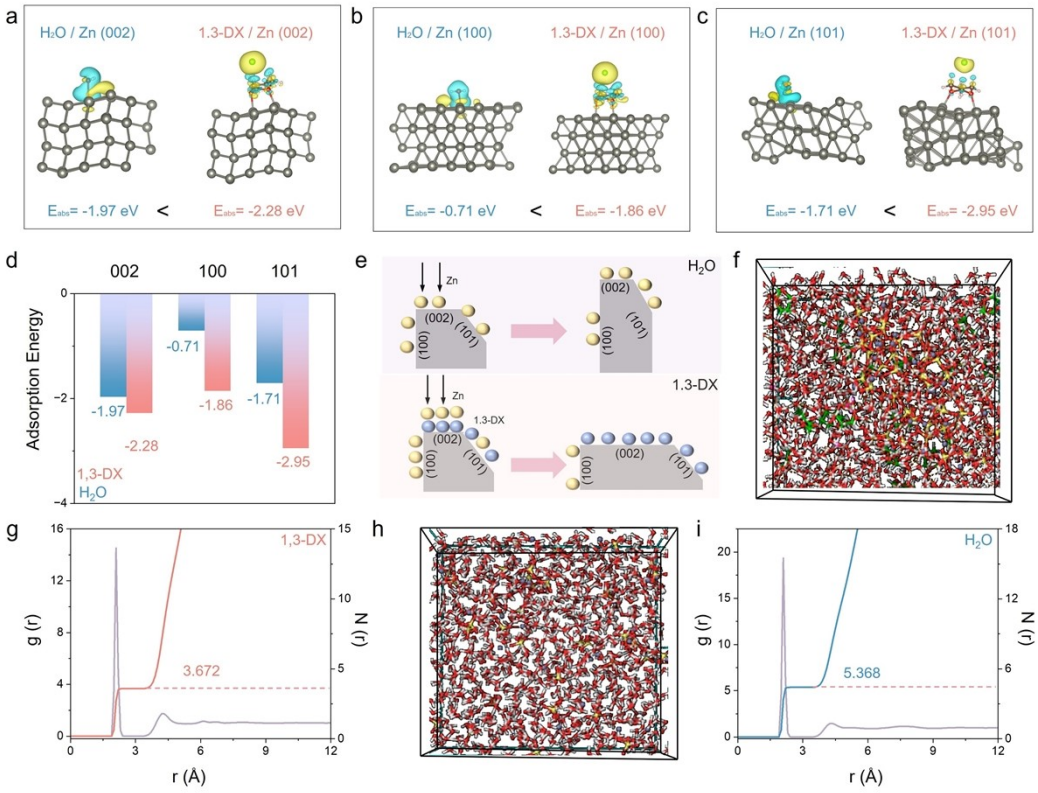

Fig. S4. Theoretical investigation of 1,3-DX as an electrolyte catalyst for regulating Zn anode mechanisms. Binding energy (a-c) of H_2O or 1,3-DX on the Zn (002), (100), and (101) facets, and the corresponding summary (d) with schematic (e) diagrams. Radial distribution functions and coordination numbers with the corresponding schematic illustrations of solvation structure of Zn^{2+}-H_2O-1,3-DX (f-g), and Zn^{2+}-H_2O (h-i).

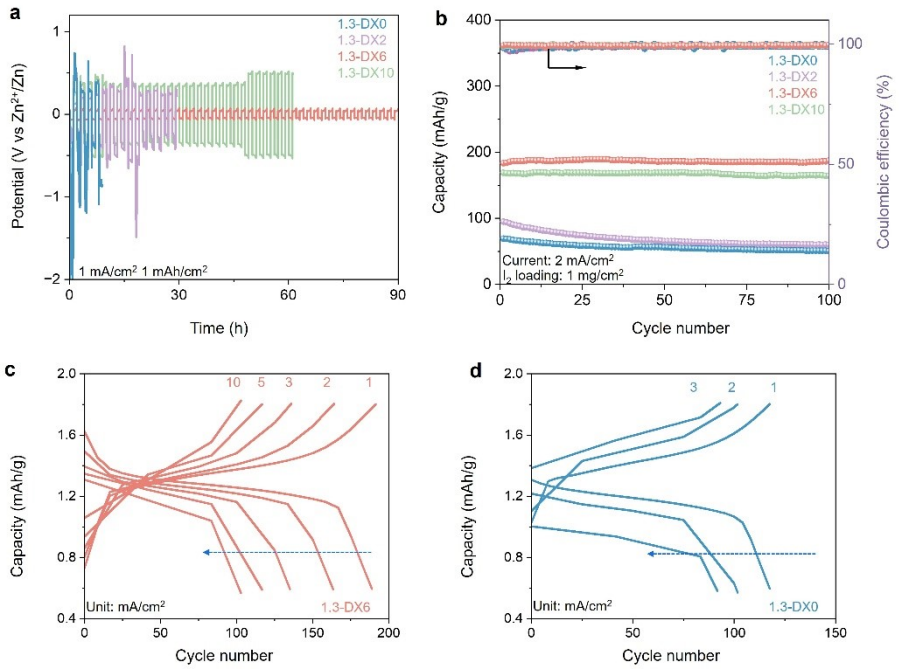

Fig. S5. Long-term cycling performance of seawater-based electrolytes with varying 1,3-DX concentrations in Zn//Zn symmetric cells (a) and Zn-I_2 cells (b). The charge/discharge profiles of Zn-I_2 cells with 1,3-DX-seawater (c) or pure seawater (d) electrolytes, respectively.

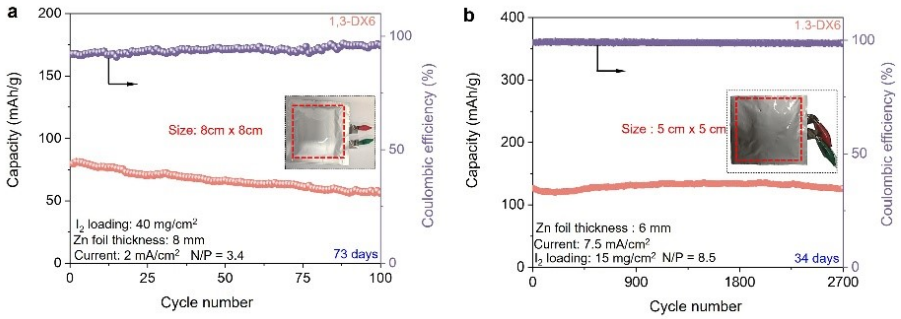

Fig. S6. The long cycling performance of Zn-I_2 cells with 1,3-DX-seawater electrolytes (a-b).

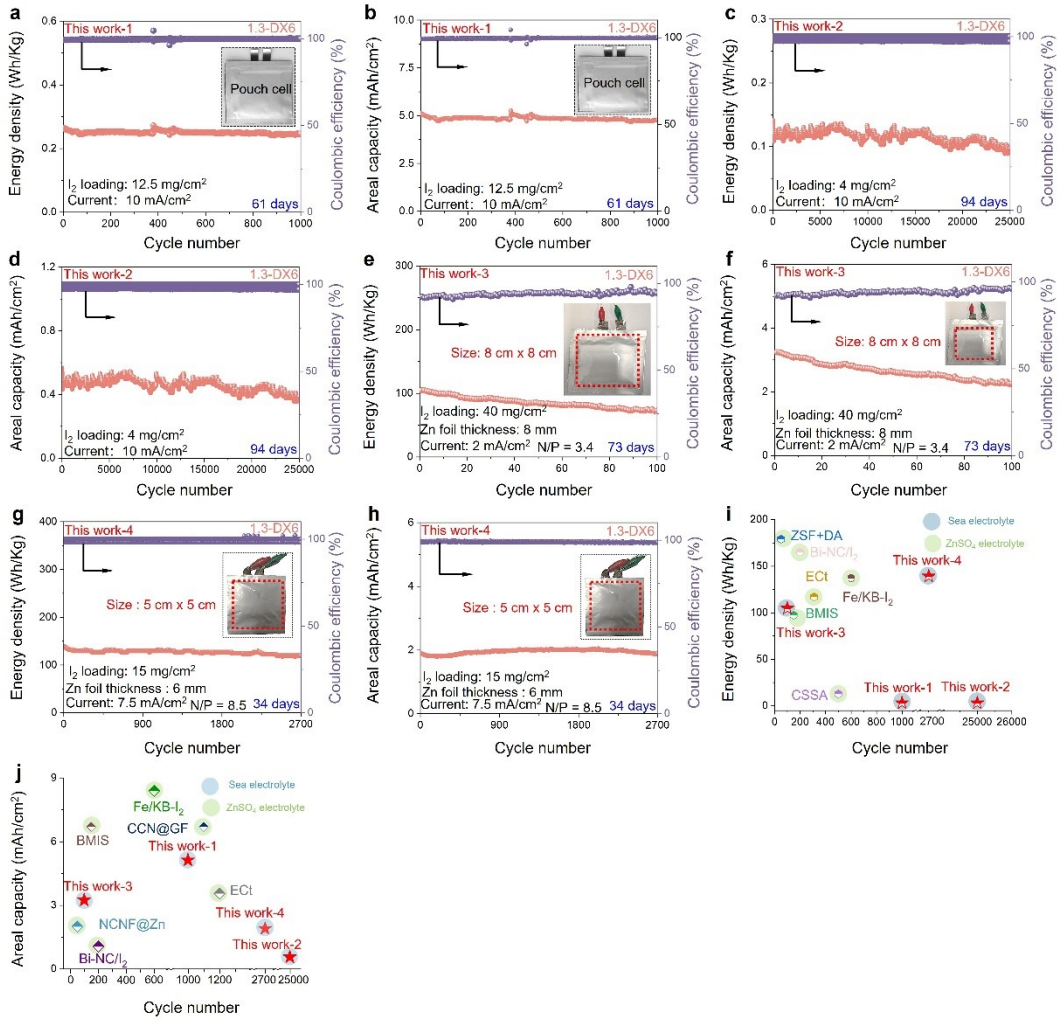

Fig. S7. The cycling performance (a-h) of with 1,3-DX6-basde Zn-I_2 cell the corresponding comparison (i-j) of cycle performances with other similar cathode (detailed description of abbreviation in Tab. S4-S5).

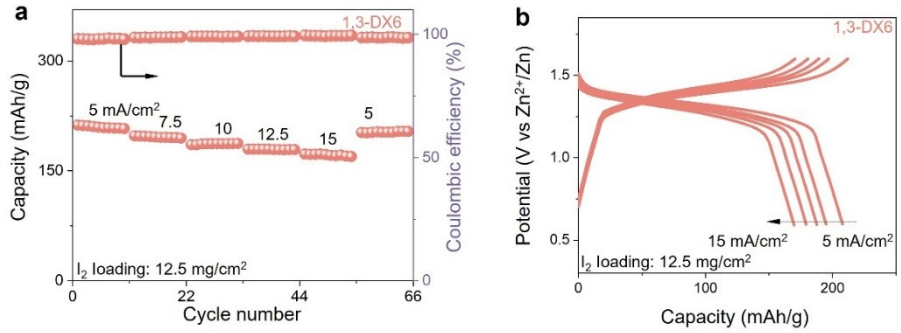

Fig. S8. Rate performance of the high-loading pouch cell (a), with corresponding voltage profiles at different current densities (b).

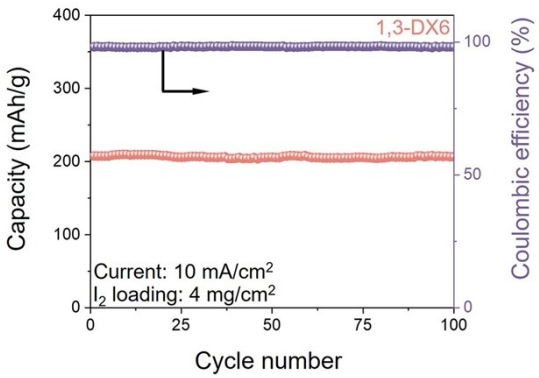

Fig. S9. Long-term cycling performance of $ZnSO_4$ electrolytes with 1,3-DX6 concentrations in the Zn-I_2 cells.

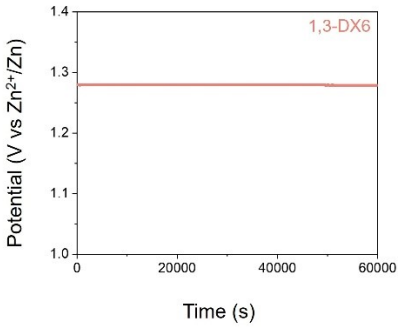

Fig. S10. Self-resting voltage and time of 1,3-DX6 cell.

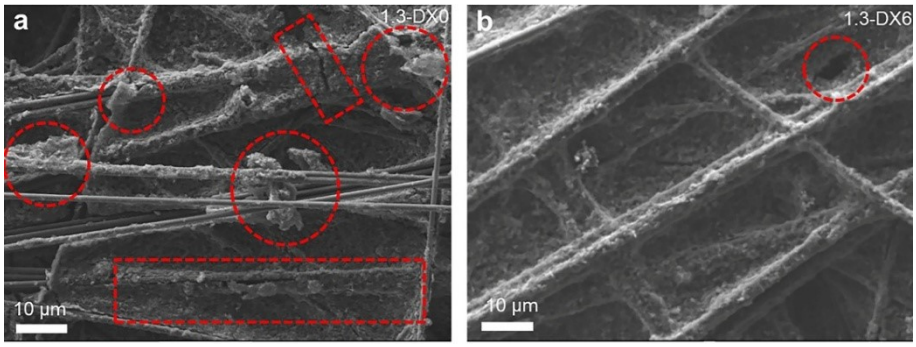

Fig. S11. The SEM images of iodine cathode with 1,3-DX-seawater (a) or pure seawater (b) electrolytes after cell cycling, respectively.

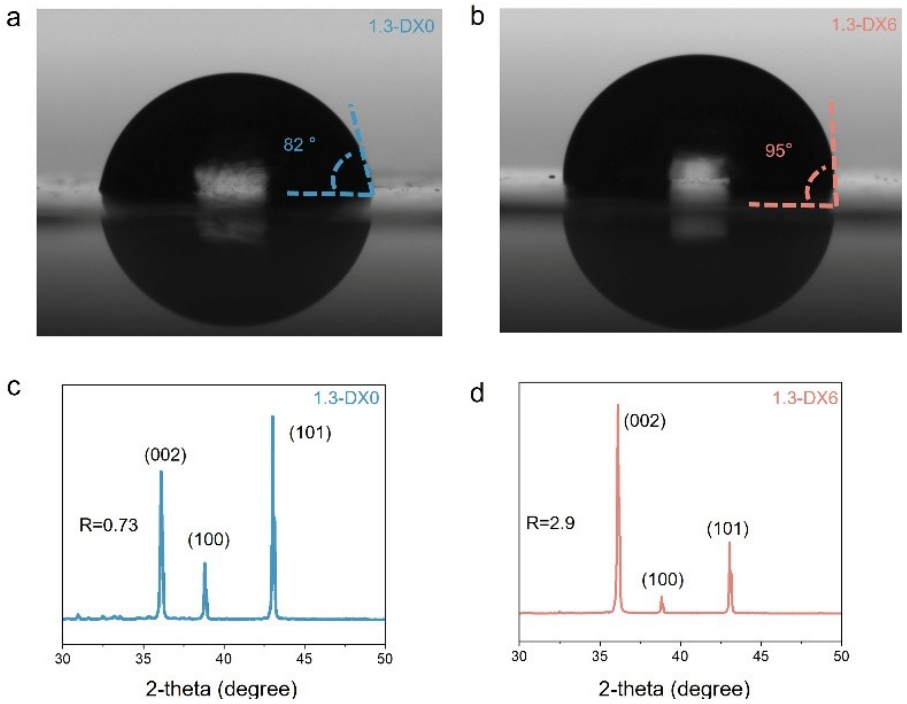

Fig. S12. The contact angles (a, b), and XRD pattern (c, d) with the corresponding peak intensity of (002)/(101) facets with the pure seawater or 1,3-DX-seawater electrolytes after cell cycling.

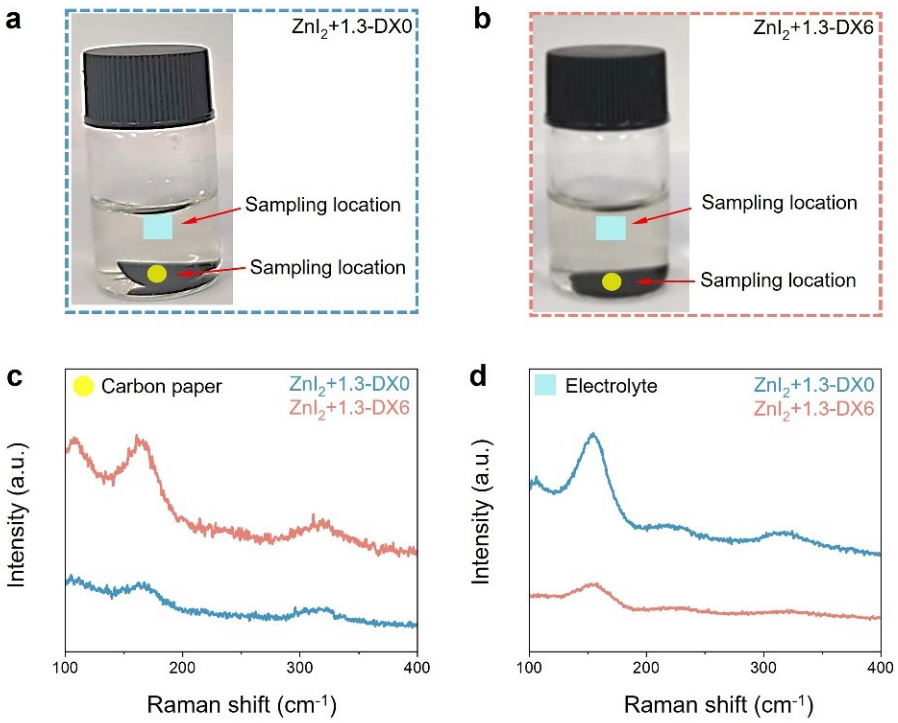

Fig. S13. Digital images of ZnI_2 adsorption tests without (a) and with (b) 1,3-DX modification. Corresponding Raman spectra (c-d).

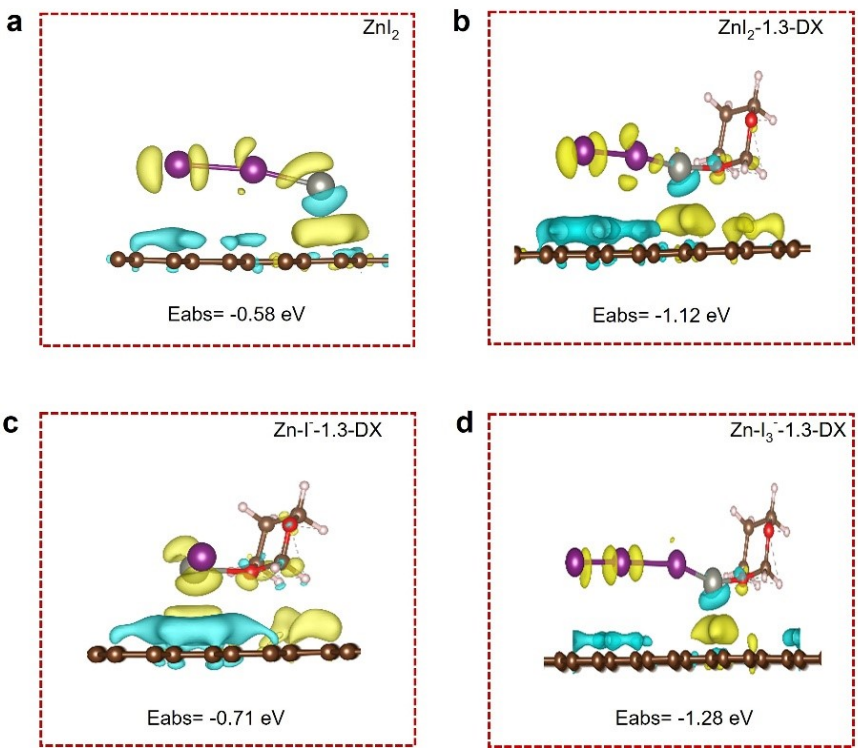

Fig. S14. Binding energy of pure I_2-Zn (a), and I_2-Zn (b), I^--Zn (c), or I_3^--Zn (d) with 1,3-DX on the current collector.

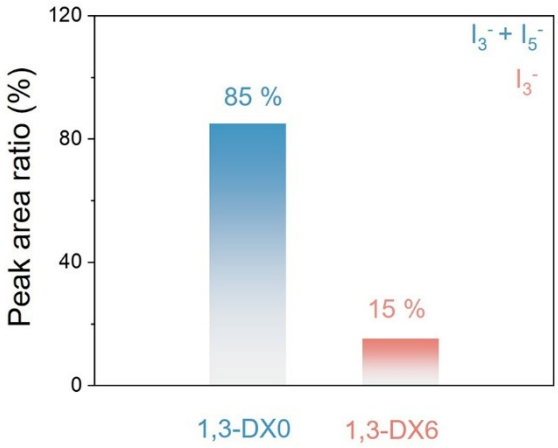

Fig. S15. In-situ Raman spectra of peak area ratios.

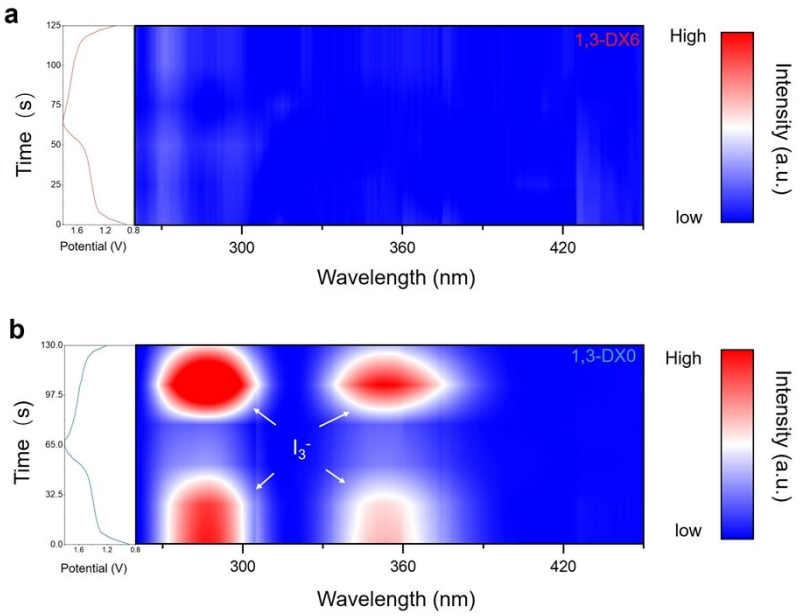

Fig. S16. In-situ UV-Vis spectra for I_3^- absorbance in 1,3-DX6 and 1,3-DX0-modified cells (a-b), respectively.

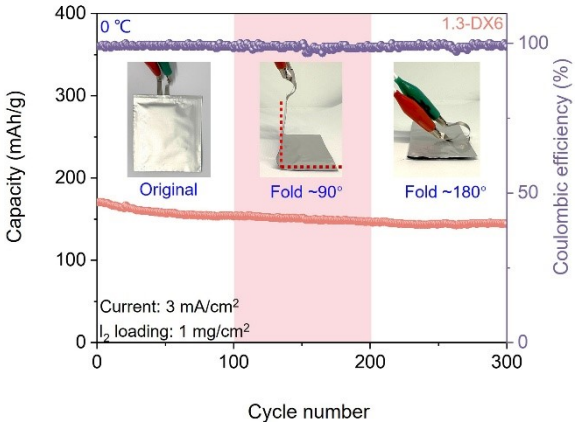

Fig. S17. Flexible cycling performance of the 1,3-DX6-based cell at 0 °C.

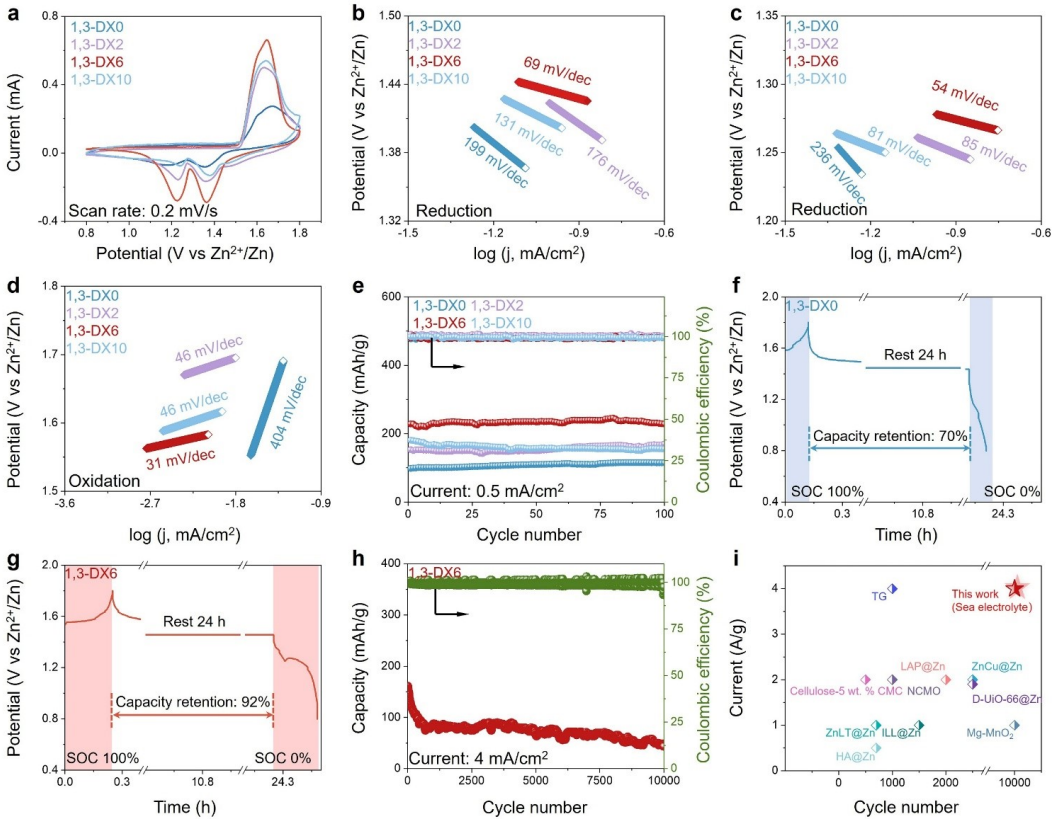

Fig. S18. Electrochemical performance of Zn-MnO_2 cells with 1,3-DX-seawater or pure seawater electrolytes. The CV curves (a) with the corresponding Tafel slopes (b-d), and the cycling performance (e). The self-discharge tests (f-g) after a rest of 24 h, and long performances (h) with the corresponding comparison (i) of cycle performances with other similar cathode (detailed description of abbreviation in Tab. S6).

Tab. S1. Diffraction peak intensity of Zn anode separate from Zn-Zn symmetric cells with various concentration 1,3-DX.

	(002)	(100)	(101)	(102)	(103)	(110)
I_0	53	40	100	28	25	21
I-0 vol%	3765	4476	23774	4963	5122	2715
I-2 vol%	3241	4408	16574	4325	3880	1384
I-4 vol%	7703	6060	34681	4445	6170	2830
I-6 vol%	6883	8198	20691	5268	4849	1569
I-8 vol%	4359	4548	16459	3955	3590	2353
I-10 vol%	2910	3046	12499	4282	2569	2209

Tab. S2. The comparison of Zn-I_2 cells with various modification recently reported.

Modification	Current density	Cycle number	Reference
6 vol%1,3-dioxane	10 mA/cm^2	25000 cycles	This work
$MXDA_2SnI_6$	1 A/g	5700 cycles	*Adv. Energy Mater. 2023, 2300922*
SC-PPS@Zn	3.2 A/g	6000 cycles	*Adv. Energy Mater. 2023, 2203790*
$ZnCl_2/H_2O$-40GBL	2 A/g	2000 cycles	*Angew. Chem. Int. Ed. 2023,62, e202301570*
PNGF	1.5 A/g	~1300 cycles	*Energy Storage Mater. 2023, 57, 557-567*
1MZSO-0.25PA	1 A/g	2500 cycles	*Energy Storage Mater. 2023, 58, 20-29*
CMK-3@I_2	0.5 A/g	1000 cycles	*ACS Materials Lett. 2022, 4,1872-1881*
P2VP	0.3 A/g	250 cycles	*Adv. Mater. 2020, 32, 2000287*
TCPP@Zn	5 A/g	5000 cycles	*Angew. Chem. Int. Ed. 2023, 62, e202217744*

Tab. S3. The comparison of Ah-level Zn-I_2 cells with various modification recently reported.

Modification	Capacity	Cycle number	Reference
6 vol%1,3-dioxane	1.02 Ah 0.4 Ah	100 cycles 2700 cycles	This work
Etched Zn-NVO	1 Ah	50 cycles	*Adv. Energy Mater. 2025, 15, 2501658*
I_2-PHNG	0.124 Ah	80 cycles	*Energy Environ. Sci., 2024, 17, 642-654*
CA-Zn	0.76 Ah	50 cycles	*Energy Storage Materials, 2025, 81, 104525*
Zn-ZSO	1 Ah	50 cycles	*Adv. Mater. 2025, 37, e11484*
3DN-C-Zn/A/VO-DMF	0.5 Ah	50 cycles	*Adv. Mater. 2022, 34, 2202188*
$D_{0.15}$-Zn	0.22 Ah	30 cycles	*Adv. Mater. 2021, 33, 2102701*

Tab. S4. The performance of energy density of Zn-I_2 cells including 1,3-DX-based device and related work in other literature.

Modification	Energy density	Cycle number	Reference
6 vol%1,3-dioxane	0.265 Wh/Kg	1000 cycles	This work
6 vol%1,3-dioxane	0.142 Wh/Kg	25000 cycles	This work
6 vol%1,3-dioxane	104.7 Wh/Kg	100 cycles	This work
6 vol%1,3-dioxane	139.2 Wh/Kg	2700 cycles	This work
BMIS	97.34 Wh/Kg	150 cycles	*J. Am. Chem. Soc. 2024, 146, 16601-16608*
CSSA	12.94 Wh/Kg	500 cycles	*Adv. Mater. 2026;0, e72959*
Ect	117 Wh/Kg	310 cycles	*Energy Environ. Sci. 2026, 19, 1551-1564*
AFe/KB-I_2	137.2 Wh/Kg	600 cycles	*Nat. Chem. 2026,18, 266-274*
ZSF+DA	179 Wh/Kg	50 cycles	*Energy Storage Mater. 2025, 83 , 104711.*
Zn/Bi-NC/I_2	165.3 Wh/Kg	200 cycles	*Chem 2026, 12, 102911.*

Tab. S5. The performance of areal capacity of Zn-I_2 cells including 1,3-DX-based device and related work in other literature.

Modification	Areal capacity	Cycle number	Reference
6 vol%1,3-dioxane	5.13 mAh/cm^2	1000 cycles	This work
6 vol%1,3-dioxane	0.57 mAh/cm^2	25000 cycles	This work
6 vol%1,3-dioxane	3.25 mAh/cm^2	100 cycles	This work
6 vol%1,3-dioxane	1.91 mAh/cm^2	2700 cycles	This work
Ect	3.57 mAh/cm^2	1200 cycles	*Energy Environ. Sci. 2026, 19, 1551-1564*
NCNF@Zn	2.01 mAh/cm^2	50 cycles	*Energy Environ. Sci. 2026, https://doi.org/10.1039/D6EE00296J*
Fe/KB-I_2	8.4 mAh/cm^2	~ 600 cycles	*Nat. Chem. 2026, 18, 266-274.*
BMIS	6.7 mAh/cm^2	150 cycles	*J. Am. Chem. Soc. 2024, 146, 16601-16608*
CCN@GF	5.8 mAh/cm^2	1100 cycles	*Adv. Mater. 2026, 38, e23132*
Zn/Bi-NC/I_2	1.07 mAh/cm^2	200 cycles	*Chem 2026, 12, 102911.*

Tab. S6. The performance of Zn-MnO_2 cells including 1,3-DX-based device and related work in other literature.

Modification	Current density	Cycle number	Reference
6 vol%1,3-dioxane	4 A/g	10000 cycles	This work
HA@Zn	0.5 A/g	700 cycles	*Energy Storage Mater. 2023, 58, 279-286*
ILL@Zn	1 A/g	1500 cycles	*Adv. Mater.* 2023, 35, 2211961
Cellulose-5 wt. % CMC	2 A/g	500 cycles	*Adv. Funct. Mater. 2023, 33, 2302098*
ZnLT@Zn	1 A/g	700 cycles	*Adv. Energy Mater. 2023, 13, 2203066*
LAP@Zn	2 A/g	2000 cycles	*Adv. Energy Mater. 2023, 13, 2204092*
TG	4 A/g	1000 cycles	*Adv. Funct. Mater. 2024, 34, 2214538*
NCMO	2 A/g	1000 cycles	*J. Mater. Chem. A,2023, 11, 11436-11444*
Mg-MnO_2	1.5 A/g	10000 cycles	*Small 2023, 19, 2301906*
ZnCu@Zn	2 A/g	2500 cycles	*Small 2023, 19, 2302995*
D-UiO-66@Zn	1.9 A/g	2500 cycles	*Nano-Micro Lett. 2023, 15, 56*